Article:
Feng, Zhengshuyi, Zhang, Tianyu, Wang, Mingkai et al. (2025) Design and implementation of an integrated scanning protocol for multimodal functional OCT. Biomedical Optics Express. pp. 4257-4272. ISSN: 2156-7085

https://doi.org/10.1364/BOE.573399

Research Article Vol. 16, No. 11 / 1 Nov 2025 / Biomedical Optics Express 4257
Biomedical Optics EXPRESS

Design and implementation of an integrated scanning protocol for multimodal functional OCT

ZHENGSHUYI FENG,[1] TIANYU ZHANG,[1] MINGKAI WANG,[2] ZHIHONG HUANG,[1] AND CHUNHUI LI[3,*]

[1]Healthcare Engineering, School of Physics and Engineering Technology, University of York, UK
[2]Photobiology Unit, NHS Tayside, Ninewells Hospital, Dundee, UK
[3]Centre for Medical Engineering and Technology, University of Dundee, UK
[*]c.li@dundee.ac.uk

Abstract: Early diagnosis of skin lesions is crucial for improving treatment outcomes. So far, based on optical coherence tomography (OCT), as a non-invasive technique, OCT structural image, optical coherence elastography (OCE), and OCT-based angiography (OCTA) have been utilized to evaluate the biomechanical properties and vascular network in in-vivo human skin. However, image registrations are the major difficulty in separating scans. Therefore, the integration of these three modalities has been achieved by a new scanning protocol to provide a comprehensive, non-invasive assessment of skin tissue, enabling more accurate differentiation between benign and malignant lesions. This study aimed to collect data for the OCT structure, OCE, and OCTA in one scanning acquisition by employing a swept-source (SS-OCT) OCT system. Eleven health participants were recruited for three positions: palm (n = 11), forearm (n = 11), and facial skin (n = 5). From OCE data, Young's modulus was calculated for the stiffness; from OCTA data, vessel area density (VAD), vessel skeleton density (VSD), vessel diameter index (VDI), and weighted Tortuosity Index (WTI) were used to evaluate the vessel network. One facial lesion dataset was collected, and the results indicated differences in the above parameters compared to healthy facial skin data. In conclusion, the new scanning protocol for integrating the structural image, OCE, and OCTA in one scan demonstrated results to calculate the parameters of the skin, which provides potential benefits for skin research and offers full aspects for dermatologists of skin disease.

1. Introduction

Skin, being the largest organ of the body, represents around 15% of total body weight and plays a critical role in defence, water retention, temperature regulation, and acts as a crucial barrier against environmental threats, pathogens, and physical damage [1,2]. Skin diseases are among the most prevalent health conditions worldwide, impacting 30% to 70% of individuals [3]. For instance, acne affects around 27% of early adolescents and nearly 93% of late adolescents [4]. In contrast, some dermatological conditions, such as scleroderma [5], are relatively rare and may involve organs of the body [6]. Skin lesions often exhibit significant variability in size and shape, ranging from millimeter to centimeter scales [7], with irregular and inconsistent forms [8]. Early diagnosis can offer treatment and recovery in time for the patients to avoid permanent skin texture and scars [4]. Visual inspection and dermoscopy are the first steps for diagnosing skin diseases. Visual inspection is subjective and generally unreliable, especially for identifying subtle or internal defects [9]. Dermoscopy's limitations in assessing depth and the heavy reliance on the clinician's diagnostic experience can potentially reduce diagnostic precision [10]. Conventional clinical methods such as the modified Rodnan skin score (mRSS) and nailfold capillaroscopy are commonly used to assess skin thickness and microvascular morphology,

#573399 https://doi.org/10.1364/BOE.573399
Journal © 2025 Received 15 Jul 2025; revised 22 Aug 2025; accepted 28 Aug 2025; published 2 Oct 2025

Biomedical Optics EXPRESS

respectively. Both methods are subjective [11–13]. For example, mRSS assessment has a steep learning curve and requires training under experienced rheumatologists to improve accuracy [11]. In addition, capillaroscopy can only image superficial capillaries using visible light with a few tens of micrometers penetration depth [13,14], and its performance is further limited in subjects with darker skin due to reduced light penetration [4]. Skin biopsy is considered the gold standard for obtaining comprehensive diagnostic information but comes with drawbacks, which include being invasive [15], delayed results due to processing time [16] and potential risks such as infection [17].

Non-invasive technique is crucial for skin disease detection because it enables safe, painless, and repeatable diagnosis without damaging the skin and causing further skin infections [18]. Ultrasound imaging can work for skin detection by detecting sound waves reflected from tissues with differing acoustic properties, it can penetrate deeper in the tissue but is limited in resolution [19]. A non-invasive imaging technique with high resolution, optical coherence tomography (OCT), has gained significant recognition over the past few decades due to its advantages, particularly its extensive applications in skin [20].

OCT provides cross-sectional images that identify different layer structures (e.g. dermis, epidermis) and reveal these structural differences, enabling accurate diagnosis of pathological changes. Hinz et al. describe OCT features of basal cell carcinoma (BCC) to accurately assess vertical tumour thickness from OCT structural image, achieving strong correlation and agreement with histopathological measurements [21]. Although OCT structural image can provide information on different tissue layers, relying exclusively on structural imaging for the diagnosis of skin diseases is inadequate, therefore, additional evaluative parameters are required to improve diagnostic accuracy [22]. Conventional structural OCT mainly provides morphological information but lacks functional contrast [23], also, structural OCT cannot provide mechanical properties or vascular information, which are increasingly recognized as important biomarkers for disease characterization [22,24].

Optical coherence elastography (OCE), is a functional modality from OCT, which inherits the advantages of OCT and can provide information on the biomechanical changes of tissues [25]. OCE utilises OCT as the image system to track and capture the propagation of surface acoustic wave (SAW) to obtain the mechanical properties information of the targeting tissue [26]. In addition, OCE has been widely applied in soft tissues [26–31], for example, OCE was applied to human prostatic tissue ex vivo, demonstrating a reliable distinction between benign and malignant tissue [25]. Additionally, Wang et al. proposed an external stimulation system combined with phase-sensitive OCT (PhS-OCT) for detecting ex-vivo human myxoma and normal fat by quantifying the Young's modulus to distinguish tumours from normal tissue [32]. Regarding skin applications, Li et al. developed PhS-OCT with mechanical impulse surface wave stimulation to non-invasively evaluate the biomechanical properties of skin in vivo, demonstrating its potential for clinical use [27]. The versatility of OCE across different tissue types highlights its significance in advancing diagnostic precision.

As another non-invasive functional extension of OCT, OCT angiography (OCTA) can demonstrate the vascular network of the targeting tissue by extracting the motion-contrasted information [33,34]. OCTA was used to scan subjects with both healthy and pathological conditions, including benign skin lesions, psoriasis, chronic graft-versus-host-disease (cGvHD), and scleroderma, effectively capturing variations in vascularization and structural features, thus aiding in the diagnosis, monitoring and understanding of these skin diseases [35]. The OCTA modality has been employed in many aspects of research previously, e.g. cutaneous wound healing [36], burn-damaged skin [37], etc.

Based on the three modalities that OCT offers, it provides comprehensive information about the lesion which includes structural layers, stiffness distribution, and microvascular characteristics. They are essential for accurate diagnosis and effective treatment monitoring. These modalities

Biomedical Optics EXPRESS

play a crucial role in providing detailed information and evaluating the lesion. Thus, combining these modalities through image registration enables comprehensive multimodal analysis for future tissue research.

Image registration is the major difficulty for OCE and OCTA results due to the lack of shared features, making registration based on common characteristics challenging. Furthermore, during the independent acquisition of OCE and OCTA, interruptions such as pauses or parameter adjustments may lead to changes or shifts in the scanning regions, thereby further increasing the difficulty of image registration. Also, the separate scanning is time-consuming for the preparation of data acquisition such as parameter resetting and re-targeting the scanning range. So far, the structural image, functional elastography, and functional angiography in one scan have yet to be developed.

A new scanning protocol is designed to integrate the OCT structural image and functional images (OCE and OCTA) in one scan to offer the image registration of the lesion and enhance the efficiency of scanning duration by 14.81%. This study aims to investigate vessel parameters from angiography and elasticity from elastography on different healthy human skin sites (e.g. palm, forearm and facial skin) by applying the new scanning protocol. This newly developed scanning protocol is expected to provide significant convenience for future data acquisition in tissue research, enhancing efficiency and optimizing the acquisition process.

2. Materials and methods

2.1. Participants recruitment

In this study, a total of eleven healthy participants (six males and five females) of Asian ethnicity were recruited for skin data acquisition. The majority (72.7%) were in the 20–29 age group, while 9.1% were in each of the 30–39, 40–49, and 50–59 age groups. All participants had no history of skin disease or other medical conditions. Data acquisition was performed in three skin sites for each participant: the forearm, the palm and the facial skin. This study was approved by Physical Sciences Ethics Committee (PSEC) of the University of York. All participants were required to sign the consent form before data acquisition.

2.2. Experimental set-up

The new scanning protocol utilized in this study was developed on a portable, lab-built swept-source optical coherence tomography (SS-OCT) with a handheld probe [29], as shown in Fig. 1(below). The data acquisition card used on the computer is an ATS-9371 from AlazarTech Inc.

A 400 kHz swept source laser (SL132120, Thorlabs Inc., Newton, MA, USA) with a center wavelength of 1300 nm and a bandwidth of 100 nm was employed in this study. The scanning probe was specifically developed to support the acquisition of structural images, along with OCE and OCTA data. The scanning probe design composed key components such as a fibre collimator, a CCD camera (UC20MPE, Spinel USA LLC, Newport Beach, CA, USA), a 2D galvo-mirror system (6210H, Cambridge Technology, Bedford, MA, USA), a piezoelectric actuator (PC4QR, Thorlabs Inc., Newton, MA, USA), an objective lens (LSM03, Thorlabs Inc., Newton, MA, USA), and a 6-inch liquid-crystal display (LCD) for real-time visualization during data acquisition.

The piezoelectric actuator was driven by a signal generator (33220A, Keysight Technologies Inc., Santa Rosa, CA, USA) with 4 kHz square wave, peak-to-peak voltage amplitude (*Vpp*) of 10 Volt, and 60% duty cycle to generate mechanical waves on the sample surface. The output signal sent to the piezoelectric actuator was enlarged by a power amplifier (QD4240, Inter-M Corporation, Korea), with a voltage gain of 4.

To ensure less attenuation of the SAW, the preload force between the piezoelectric actuator end and the targeting tissue is usually pressed around 30 μm. The contact status between the

Biomedical Optics EXPRESS

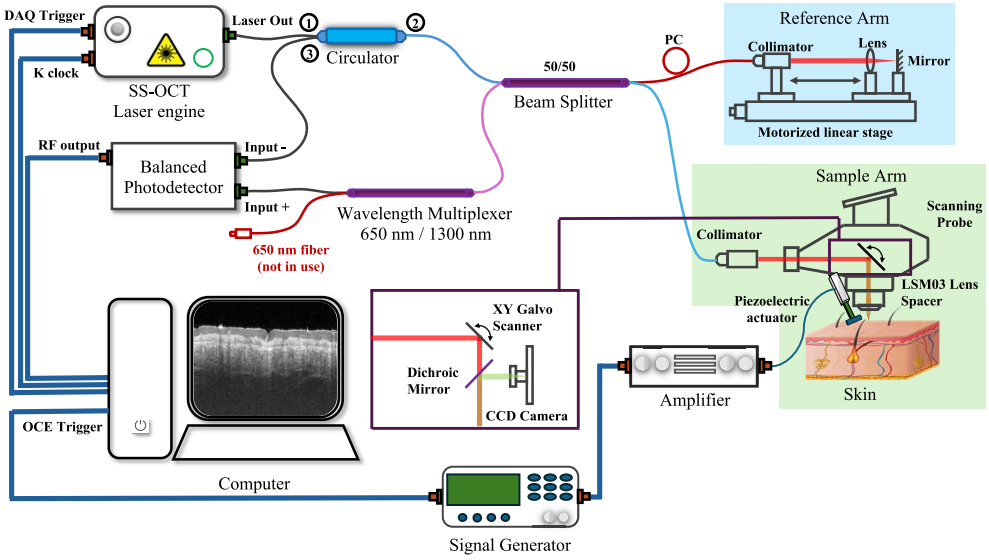

Fig. 1. Schematic diagram of SS-OCT system with probe. PC, polarization controller; CCD, Charge-coupled device.

targeting sample and the piezoelectric actuator tip could be monitored in real time to ensure the stimulation conditions were all constant during the whole data collection for each subject. For synchronization, the signal generator was set to external trigger mode and triggered by the SS-OCT system.

2.3. *Scanning protocol*

The timing schematic of the new scanning protocol is shown in Fig. 2. In Fig. 2, t_data denotes the data acquisition status signal generated by the acquisition card. When t_data is at a high level, the acquisition card is actively sampling data, whereas a low level indicates that the acquisition process is paused. The x galvo mirror and y galvo mirror represent the voltage of the galvo-mirror driver. High level of OCE trigger describes the signal sent to the signal generator which is set to external trigger mode.

To evaluate the viability of the new scanning protocol, the scanning protocol was applied to all skin sites for each participant. For this new scanning protocol, since structural data, OCE data and OCTA data were integrated in one scanning. Therefore, only a single 3D volume dataset will be generated during the data acquisition. Both the X-scan mirror and Y-scan mirror of the galvo-mirror system were employed for the 3D volume dataset collection. OCE data included 600 A-lines (one M-scan, represented as M) at the same location. An A-line could investigate the target sample's depth information. One B-scan consisted of 100 M-scans. Then the slow-axis of the galvo-mirror system would manipulate the laser along with the Y-axis to generate part of the whole dataset with dimensions of $384 \times 100 \times 100 \times 600$ ($Z \times X \times Y \times M$ in pixels) for OCE data. Z, X and Y are one axial and two lateral spatial dimensions, respectively. For OCTA data, the X-scan mirror as the fast-axis to scan multiple A-lines along the X-axis with 6 repeats (N), the angiography information of the same location could be captured. Then Y-scan mirror enables line-by-line scanning along the Y-axis to collect 3D datasets. Therefore, the rest of the whole dataset is OCTA data, with dimensions of $384 \times 600 \times 600 \times 6$ ($Z \times X \times Y \times N$ in pixels). The duration of the whole data collection will take approximately 23 seconds with a field of view 5.1 mm $\times$ 5.1 mm and around 1.7 mm penetration depth.

Biomedical Optics EXPRESS

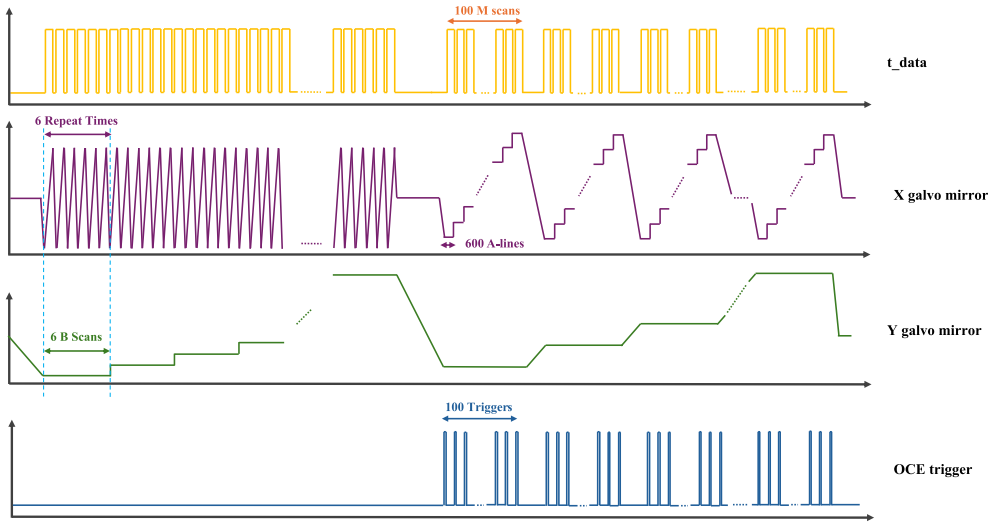

Fig. 2. Timing schematic of new scanning protocol of SS-OCT system.

2.4. Data processing

As the skin thickness and signal attenuation will depend on different individuals, therefore, to evaluate vessel parameters accurately, the automatic Depth of Interest (DOI) selection algorithm was employed to obtain two individual layers [38]. The equations to calculate several vascular parameters are shown below:

VAD, the vessel area density, demonstrates the ratio of vessel area to whole image area [39], as shown in Eq. (1).

$$VAD = \frac{\sum_{x=1,\,y=1}^{n} V_{(x,y)}}{\sum_{x=1,\,y=1}^{n} I_{(x,y)}} \times 100\% \tag{1}$$

where $V_{(x,y)}$ is the total area of the vessel in pixels, $I_{(x,y)}$ is the whole area of the image in pixels. Assume the entire area of the image is a matrix with a size of $n \times n$. (x, y) presents the pixel coordinates in the vessel image [38]. In this calculation, the result value considers both vessel length and vessel diameter. However, the value might provide incorrect information if vessel dilation (vessel diameter increases) and blood perfusion decrease happen at the same time [40].

VSD presented vessel skeleton density in percentage which can calculated by Eq. (2) [38].

$$VSD = \frac{\sum_{x=1,\,y=1}^{n} S_{(x,y)}}{\sum_{x=1,\,y=1}^{n} I_{(x,y)}} \times 100\% \tag{2}$$

where $S_{(x,y)}$ is the vessel skeleton in pixels, $I_{(x,y)}$ is the total area of the image in pixels. Vessel diameter was not taking account in this parameter calculation, only focus if the vessel existed or not [40].

VTI, vessel tortuosity index, represents the tortuosity of vessels, which involves the ratio of each vessel segment length and straight distance, shown in Eq. (3) [38,41].

$$\mathrm{VTI} = \left(\frac{L}{D} - 1\right) \times 100 \tag{3}$$

where L and D are the length and straight distance of each vessel skeleton segment separately. The results would be a matrix for each vessel skeleton segment.

Biomedical Optics EXPRESS

VDI, vessel diameter index, the equation shown in Eq. (4).

$$\mathrm{VDI} = \frac{\sum_{x=1,\,y=1}^{n} 2 \cdot \min\limits_{(u,v) \in \bar{I}} \sqrt{(x-u)^2 + (y-v)^2} \cdot S_{(x,y)}}{\sum_{x=1,\,y=1}^{n} S_{(x,y)}} \tag{4}$$

where (x, y) presents the pixel coordinates in the vessel image, (u, v) range overall pixel coordinates in the inverted binary image, $\bar{I}$ is the inverted binary image and $S_{(x,y)}$ is the vessel skeleton in pixels. The unit of VDI is pixels, all vessel diameter result has been converted into a micrometer unit [40].

As the vessel tortuosity was taken into account the blood vessel research, the vessel diameter has to be considered. Therefore, the weighted TI (WTI) method should be calculated by using Eq. (5) [38].

$$\mathrm{WTI} = \frac{\sum_{m=1}^{M} \mathrm{VD}I_m \times \mathrm{VT}I_m}{\sum_{m=1}^{M} \mathrm{VD}I_m} \tag{5}$$

where M is the total number of vessel segments, $\mathrm{VD}I_m$ and $\mathrm{VT}I_m$ are the vessel diameter index and vessel tortuosity index of the m *th* vessel segment.

For visualization of the blood vessel network of targeting tissue, all datasets went through Fourier transform, then performed windowed eigen-decomposition (wED) algorithm for processing 4D dataset into 3D dataset to obtain signals of angiography and motion artifact reduction [33]. En-face projection was generated from the 3D dataset by applying 3D Maximum Intensity [38,42]. The en-face grey scale angiography was processed into a binary image. The Hessian filter [39,43], adaptive threshold [44] and Otsu global threshold [45] were combined to reduce the noise for the binary image. Then the skeleton image of the blood vessels which was presented in single pixel wide line was obtained to provide information on the vessel length and vessel density. Based on the images above, other parameters such as vessel diameter and vessel tortuosity could be calculated. The outline of OCTA quantitative analysis algorithm is shown in Fig. 3.

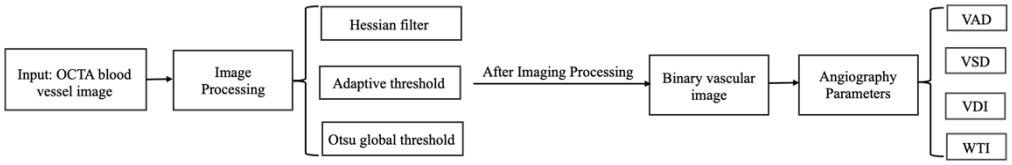

Fig. 3. The flow chart of OCTA quantitative analysis algorithm. VAD: vessel area density; VSD: vessel skeleton density; VDI: vessel diameter index; WTI: weighted tortuosity index.

The SAW velocity was estimated by tracking the propagating wave in the tissue using a time-of-flight algorithm, which calculates time and displacements along the propagation direction. This process involved applying the Fourier transform to determine the time lag of the phase data and fitting a linear model to these lags. In one specific frequency, the SAW velocity (C_{SAW}) could be expressed below in Eq. (6) [46]:

$$C_{SAW}(\omega) = \frac{\omega \Delta r}{\Delta \varphi} \tag{6}$$

where Δr is wave path, also known as the displacement distance, $\Delta\varphi$ is phase delay, ω is the angular frequency. Based on the extraction of SAW velocity, the relationship of Young's modulus

Biomedical Optics EXPRESS

(E) with SAW velocity (C_{SAW}) is described in Eq. (7) [46,47]:

$$C_{SAW} = \frac{0.87 + 1.12\nu}{1 + \nu}\sqrt{\frac{E}{2\rho(1 + \nu)}} \tag{7}$$

where ρ denotes the density of skin tissue, which is 1060 kg/m^3, C_{SAW} is SAW velocity, ν represents Poisson's ratio with 0.45 [30,48] and E is Young's modulus.

All en-face projection view images from angiography and cross-sectional elastography were saved for further 3D reconstruction.

All data was acquired by the customized LabVIEW interface (version 2016, NI, National Instruments, Austin, TX, USA) and was saved in the laboratory PC for further data processing in MATLAB (R2019b, The MathWorks, Inc., Natick, MA, USA). To ensure reliable results, three scans were required for data acquisition on each position for each participant.

3. Result

3.1. Quantitative analysis in healthy body data

The results of the forearm from one healthy participant are shown in Fig. 4. Figure 4(A) demonstrates the en-face structural projection in gray-scale of the forearm; Fig. 4(B) shows OCTA en-face projection of forearm; Fig. 4(C) illustrates the image from CCD camera; Fig. 4(D) displays the OCE en-face projection of forearm.

Regarding to the quantitative assessment of the vessel network for palm and forearm, the data were segmented by the automatic DOI selection algorithm in DOI 1 and DOI 2, as shown in Fig. 5.

The OCTA en-face projection view of DOI 1 and DOI 2 in gray-scale are shown in Fig. 5(A) to Fig. 5(B) for palm. The corresponding binary vascular images are shown in Fig. 5(C) to Fig. 5(D). Also, for palm, the tortuosity index skeleton images are displayed in Fig. 5(E) to Fig. 5(F), with quantitative tortuosity index heatmap depicted in Fig. 5(G) to Fig. 5(H). Figure 5(I) to Fig. 5(J) illustrate the vessel density heatmap for palm in DOI 1 and DOI 2. Additionally, Fig. 5(K) to Fig. 5(L) present the vessel diameter heatmaps. Similarly, Fig. 5(M) to Fig. 5(X) present the OCTA en-face projection view in gray-scale and quantitative results for the forearm.

Currently, for eleven healthy volunteers, the quantitative assessment of vessel and Young's modulus of palm and forearm of total participants were all listed in Table 1 and Table 2, separately.

Table 1. Quantitative vessel analysis of total healthy participants (n = 11) on palm

Function	Angiography - DOI 1				Angiography – DOI 2				Elastography
Quantitative Parameters	VSD	VAD	VDI (μm)	WTI	VSD	VAD	VDI (μm)	WTI	Young's modulus (kPa)
Mean	4.37%	15.10%	40.78	17.07	3.15%	14.32%	51.97	13.82	145.80
Standard Deviation	1.74%	5.50%	1.42	2.83	0.96%	3.93%	1.97	2.55	30.42
Lower 95%	3.76%	13.15%	40.27	16.07	2.81%	12.92%	51.27	12.91	135.42
Upper 95%	4.99%	17.05%	41.28	18.07	3.50%	15.71%	52.57	14.72	156.18

Based on the quantitative assessment for palm in Table 1, several parameters were calculated: in DOI 1, the output of VSD, VAD, VDI and WTI are 4.37%, 15.10%, 40.27 μm and 17.07; in DOI 2, the output of the above values are 3.15%, 14.32%, 51.97 μm and 13.82. Compared the parameters of DOI 1 and DOI 2, the VSD and VAD show a decreasing trend in DOI 2, with 27.92% and 5.17%. VDI demonstrates a 27.44% increase in DOI 2. Compared with DOI 1, WTI indicated a 19.04% decrease in DOI 2.

Biomedical Optics EXPRESS

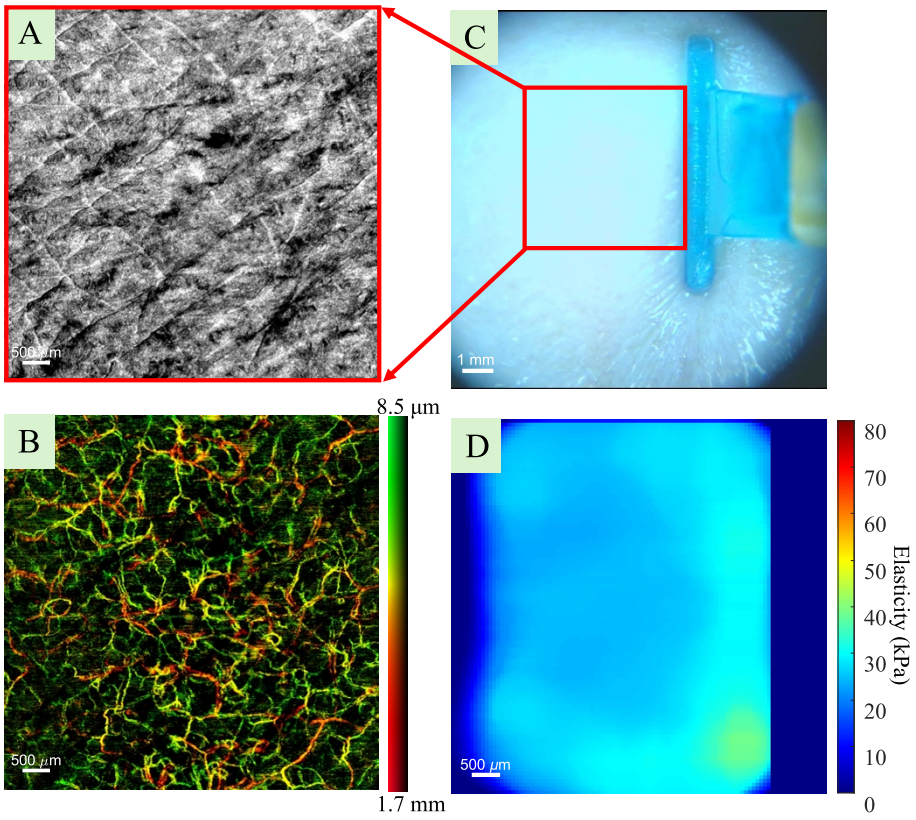

Fig. 4. Results of forearm from participant. (A) en-face structural projection image in gray-scale; (B) OCTA en-face projection image; (C) image from CCD camera; (D) OCE en-face projection image.

Table 2. Quantitative vessel analysis of total healthy participants (n = 11) on forearm

Function	Angiography - DOI 1				Angiography – DOI 2				Elastography
Quantitative Parameters	VSD	VAD	VDI (μm)	WTI	VSD	VAD	VDI (μm)	WTI	Young's modulus (kPa)
Mean	3.85%	12.62%	39.40	16.33	2.14%	9.19%	49.98	12.97	40.36
Standard Deviation	1.40%	4.54%	1.45	1.69	0.78%	3.16%	2.99	1.80	11.65
Lower 95%	3.32%	10.89%	38.85	15.68	1.85%	7.99%	48.85	12.27	36.12
Upper 95%	4.38%	14.35%	39.95	16.97	2.44%	10.39%	51.12	13.67	44.61

Biomedical Optics EXPRESS

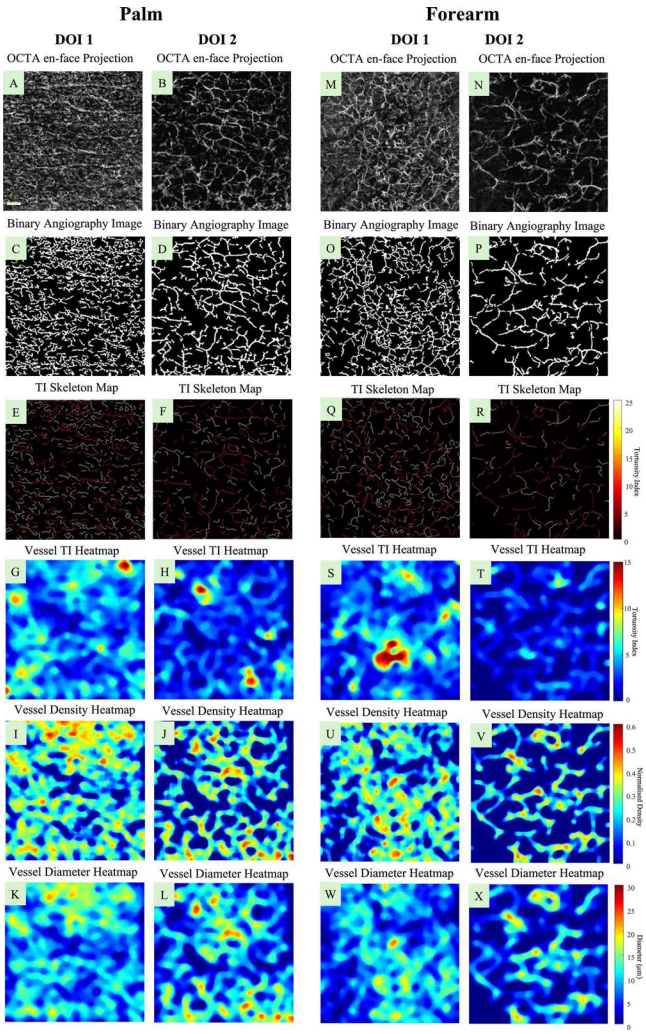

Fig. 5. The quantitative assessment results of the vessel network for palm and forearm. (A) OCTA en-face projection image in gray-scale of DOI 1 on palm; (B) OCTA en-face projection image in gray-scale of DOI 2 on palm; (C) Binary angiography image of (A); (D) Binary angiography image of (B); (E) The TI skeleton map of (A); (F) The TI skeleton map of (B); (G) The quantitative vessel TI heatmap of (A); (H) The quantitative vessel TI heatmap of (B); (I) The quantitative vessel density heatmap of (A); (J) The quantitative vessel density heatmap of (B); (K) The quantitative vessel diameter heatmap of (A); (L) The quantitative vessel diameter heatmap of (B); (M) OCTA en-face projection image in gray-scale of DOI 1 on forearm; (N) OCTA en-face projection image in gray-scale of DOI 2 on forearm; (O) Binary angiography image of (M); (P) Binary angiography image of (N); (Q) The TI skeleton map of (M); (R) The TI skeleton map of (N); (S) The quantitative vessel TI heatmap of (M); (T) The quantitative vessel TI heatmap of (N); (U) The quantitative vessel density heatmap of (M); (V) The quantitative vessel density heatmap of (N); (W) The quantitative vessel diameter heatmap of (M); (X) The quantitative vessel diameter heatmap of (N); The scale bar represents 500 μm, the scale bar in Fig. 5(A) represents all scale bars in this Fig. 5.

Biomedical Optics EXPRESS

Similarly, based on Table 2, the VSD are 3.85% and 2.14% in DOI 1 and DOI 2, respectively. In DOI 2, the forearm's VAD is 9.19%, lower than VAD in DOI 1, which is 12.62%. VDI in DOI 1 (39.40 μm) shows a decreasing trend in DOI 2 (49.98 μm). Besides, for WTI, DOI 1 (16.33) is higher than DOI 2 (12.97), with a 20.58% increase.

The Young's modulus values were determined by the group velocity, the group velocity are 6.75 ± 0.68 m/s and 3.55 ± 0.48 m/s with corresponding Young's modulus are 145.80 ± 30.42 kPa and 40.36 ± 11.65 kPa for palm and forearm, respectively.

3.2. Quantitative analysis of facial skin

Five healthy participants were involved in data acquisition for facial skin. The quantitative assessment of the vessel network and Young's modulus of facial skin of total participants were all listed in Table 3.

Table 3. Quantitative vessel analysis of total healthy participants (n = 5) on healthy facial skin

Function	Angiography - DOI 1				Angiography – DOI 2				Elastography
Quantitative Parameters	VSD	VAD	VDI (μm)	WTI	VSD	VAD	VDI (μm)	WTI	Young's modulus (kPa)
Mean	4.49%	15.15%	39.56	17.99	2.86%	14.41%	54.38	15.51	56.88
Standard Deviation	1.45%	5.05%	0.89	1.81	0.88%	4.24%	1.78	2.28	13.30
Lower 95%	3.15%	10.48%	38.74	16.33	2.04%	10.48%	52.73	13.40	49.02
Upper 95%	5.83%	19.82%	40.38	19.67	3.68%	18.33%	56.03	17.62	64.74

However, one abnormal dataset was scanned from another participant with the facial lesion, Fig. 6 shows the wave propagation of SAW at different time points in the facial lesion dataset. Figure 6(A) to Fig. 6(D) illustrates the wave propagation at time 62.5 μs, 90 μs, 280 μs and 327.5 μs, respectively.

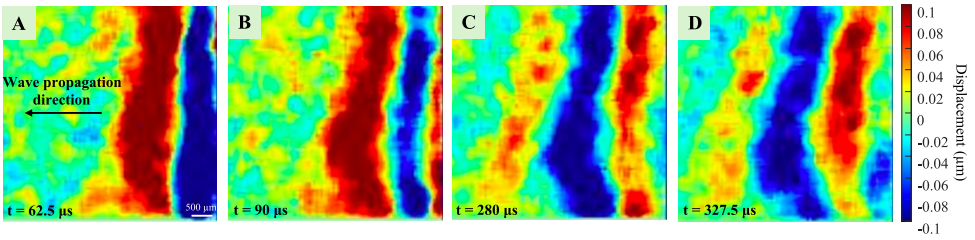

Fig. 6. Wave propagation of SAW at different time points in the facial lesion dataset. (A) Time = 62.5 μs; (B) Time = 90 μs; (C) Time = 280 μs; (D) Time = 327.5 μs.

The result of the facial lesion dataset is shown in Fig. 7, which includes en-face structural projection in gray-scale (Fig. 7(A)); OCTA en-face projection (Fig. 7(B)); image from CCD camera (Fig. 7(C)); OCE en-face projection (Fig. 7(D)) of facial lesion. The scanning range was shown in the red-dash square (Fig. 7(C)).

In this facial lesion data (highlighted in white dashed square), the mean group velocity is 10.2 m/s and the average Young's modulus is approximately 323.45 kPa, indicating an increasing trend of 468.65% compared with healthy facial skin.

After previewing the result, Fig. 8 demonstrates OCTA en-face projection in gray-scale (Fig. 8(A) and Fig. 8(B)), tortuosity index skeleton map (Fig. 8(C) and Fig. 8(D)) and the heatmaps of vessel density (Fig. 8(G) and Fig. 8(H)), vessel diameter (Fig. 8(I) and Fig. 8(J)) and

Biomedical Optics EXPRESS

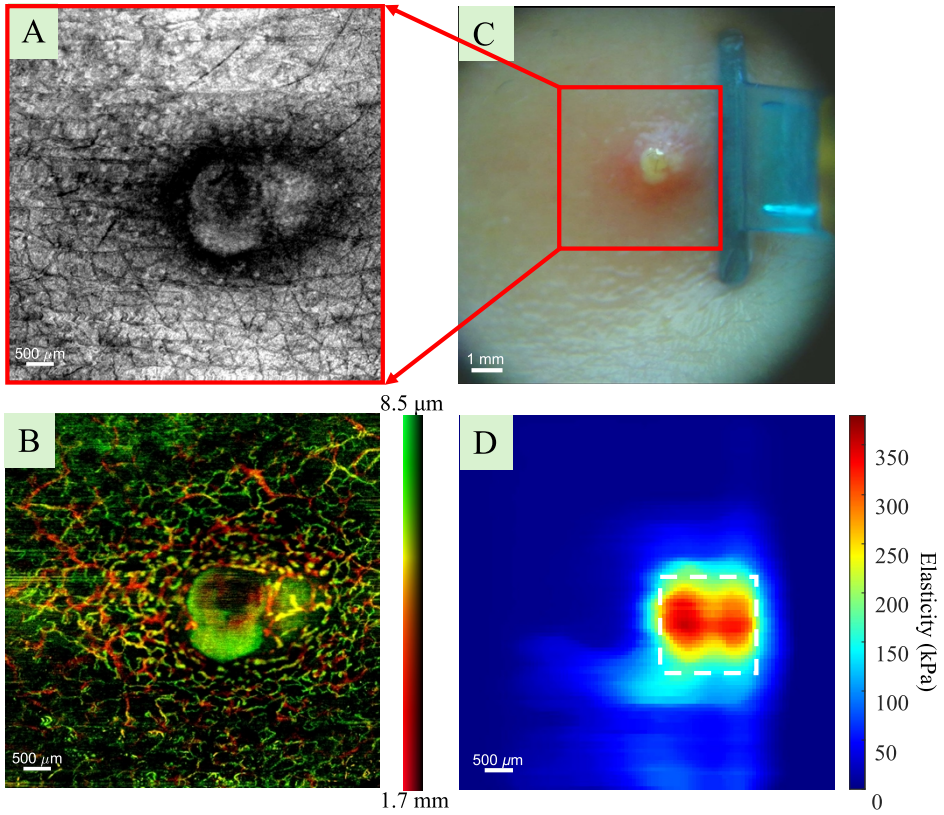

Fig. 7. Results of the facial lesion from a participant. (A) en-face structural projection image in gray-scale; (B) OCTA en-face projection image; (C) image from CCD camera; (D) OCE en-face projection image.

tortuosity index (Fig. 8(E) and Fig. 8(F)) for DOI 1 and DOI 2 for facial acne. The facial acne site was highlighted in Fig. 8(A) and Fig. 8(B) with the yellow dashed line.

By comparing the lesion area with the healthy skin: for DOI 1, the VSD of the facial lesion area is 3.27%, which is lower than the healthy facial skin VAD of 4.49% since the vessel is missing of the facial lesion area. The VAD of the facial lesion area is 10.73% lower than the healthy facial skin area, showing a decreasing trend, with 41.19%, performing lack of vessel segments in the facial lesion area. VDI of DOI 1 is 38.14 μm in the facial acne area, which is lower than that of the healthy facial skin region (39.56 μm), suggesting narrower vessel segments in the facial lesion area. The WTI of DOI 1 is 18.40, which is higher than the health mean value of 17.99, indicating that tortuosity is higher in facial lesion region.

In DOI 2, the VSD and VAD are 4.35% and 19.63%, which is higher than the healthy values of 2.86% and 14.41%, respectively, suggesting an increasing trend of vessel segmentation in facial lesion region. VDI (51.32 μm) displays a decreasing trend, lower than that of the healthy facial skin region (54.38 μm). The facial lesion area of WTI is 15.93, higher than that of in healthy value (15.51), showing larger tortuosity in the deeper layer of the vessel network in the facial lesion area.

This example reveals differences between the facial lesion region with the healthy facial skin in mechanical properties and microvascular parameters, such as Young's modulus, vessel density, vessel diameter and vessel tortuosity. However, more abnormal datasets need to be involved

Biomedical Optics EXPRESS

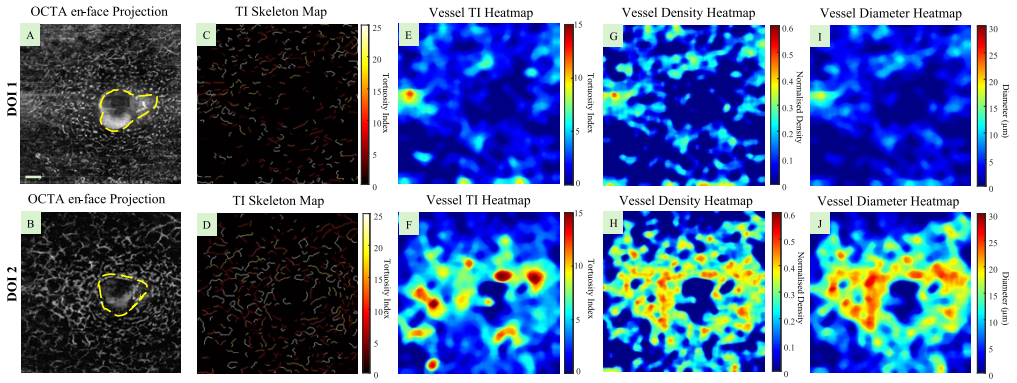

Fig. 8. The quantitative assessment results of the vessel network for facial lesion. (A) OCTA en-face projection image in gray-scale of DOI 1 on facial lesion; (B) OCTA en-face projection image in gray-scale of DOI 2 on facial lesion; (C) The TI skeleton map of (A); (D) The TI skeleton map of (B); (E) The quantitative vessel TI heatmap of (A); (F) The quantitative vessel TI heatmap of (B); (G) The quantitative vessel density heatmap of (A); (H) The quantitative vessel density heatmap of (B); (I) The quantitative vessel diameter heatmap of (A); (L) The quantitative vessel diameter heatmap of (J); The scale bar represents 500 μm, the scale bar in Fig. 8(A) represents all scale bars in this Fig. 8.

due to individual variability. The example dataset is merely intended to demonstrate the new scanning protocol in this study has the potential to diagnose the abnormal skin status.

4. Discussion

In this study, we built a new scanning protocol to integrate the OCT structural image, OCE and OCTA in one scan for improving SS-OCT system performance. The new scanning protocol was applied on in-vivo human healthy and lesion skin. The quantitative assessment methods, involving Young's modulus, VAD, VSD, VDI and WTI, these five parameters were utilized to evaluate the biomechanical properties of the targeted skin region. Three positions (palm, forearm and facial skin) were scanned from healthy participants. Also, for comparison, one facial lesion data was acquired to demonstrate the difference between facial skin lesion and healthy facial skin in stiffness and vessel parameters analysis.

The new scanning protocol basically overcomes the registration problem for different OCT functions (structural imaging, OCE, and OCTA) and improves scanning efficiency by 14.81% for the pure data acquisition time. Moreover, when considering the additional parameter setting and participant positioning steps, the overall visiting time for each participant previously exceeded 15 minutes, whereas the optimized protocol helps minimize these extra adjustments. The image registration of skin lesions enables accurate alignment of OCT data with multi-modality, improving diagnostic precision and facilitating consistent monitoring the lesion area over time.

In addition, this is the first time combining elastography and angiography modalities for facial lesion in vivo participants. This provides potential benefits for skin research and offers a non-invasive technique for dermatologists to diagnose skin lesions.

Regarding relevant studies, only one parameter was employed to evaluate skin, for instance, VAD [4,49], elasticity [50]. However, quantitative assessment methods in this study provide full aspects of both elastography and angiography for skin evaluation.

Biomedical Optics EXPRESS

Based on the previous studies, in Young's modulus site, the results of palm and forearm are 146 ± 30 kPa and 40 ± 12 kPa, respectively, which has a similar value to the literature, which was displayed in Table 4.

Table 4. Young's Modulus of skin at different sites (palm and forearm) and the corresponding reference value from the literature.

Palm			
Research	Number of subjects	Age Range	Young's Modulus (kPa)
This Research	**11**	**24 - 60**	**146 ± 30**
Zhou [51]	11	22 - 36	212 ± 78
Zhang [52]	10	46 - 61	108 ± 48
Feng [30]	10	21 - 30	164 ± 42
Forearm			
Research	Number of subjects	Age Range	Young's Modulus (kPa)
This Research	**11**	**24 - 60**	**40 ± 12**
Zhou [51]	11	22 - 36	32 ± 11
Zhang [52]	10	46 - 61	42 ± 32
Wakhlu [53]	16	41 ± 12	16 - 26
Boyer [54]	4	23 - 28	13 - 33
Feng [30]	10	21 - 30	41 ± 22

By comparing the vessel parameters in palm and forearm, we noticed that palm and forearm share the similar values in VSD (palm-DOI 1: 4.37%, DOI 2: 3.15%; forearm-DOI 1: 3.85%, DOI 2: 2.14%), VDI (palm-DOI 1: 40.78 μm, DOI 2: 51.97 μm; forearm-DOI 1: 39.40 μm, DOI 2: 49.98 μm) and WTI (palm-DOI 1: 17.07, DOI 2: 13.82; forearm-DOI 1: 16.33, DOI 2: 12.97) except VAD (palm-DOI 1: 15.10%, DOI 2: 14.32%; forearm-DOI 1: 12.62%, DOI 2: 9.19%), suggesting that these two skin sites have the similar vessel distribution, but palm has greater capillary density than any other parts of body [55]. For comparison, the value of VAD (DOI 1: 10.73%) in the superficial layer showed a decreasing trend for the facial lesion data analysis, demonstrating the loss of capillary missing and damage of the structural tissue [56]. The WTI of the facial lesion (DOI 1: 18.40%; DOI 2: 15.93%) was higher than the healthy facial skin, indicating the higher tortuosity of the facial lesion tissue, which may be due to the development of the facial lesion inflammation and the healing repair process for the facial skin [57].

Also, the average Young's modulus of the facial lesion (323.45 kPa) is higher than that of healthy facial skin (56.88 kPa), suggesting the facial lesion has higher stiffness and the biomechanical properties of the lesion area were changed compared with the healthy skin area [28].

So our quantitative assessment of the vessel network and biomechanical properties comparison could provide the benefit of distinguishing the facial skin lesion.

Several limitations should be considered in future work. Firstly, although the Young's modulus results agreed with the other studies, the results may not be fully accurate since the limited participants in our study. Therefore, larger numbers of participants should be involved in both healthy tissue and lesion tissue to build a skin database for further skin research. Meanwhile, the age range and different individuals also get affected with the results. Considering the whole duration time of data acquisition and motion artifacts reduction in OCE, deep learning, e.g. super-resolution and reconstruction, has the benefit of reducing both scanning duration time and motion artifacts for future work. Also, the acne lesion undergoes various stages of development. Vascular parameters such as vessel density are likely to exhibit corresponding changes at each stage [4]. Therefore, it would be highly beneficial to analyze different vessel parameters and

Biomedical Optics EXPRESS

mechanical properties alteration within the same acne lesion in future work, as this will provide valuable insights for acne research.

5. Conclusion

In this study, a new scanning protocol was designed, and eleven participants were scanned by using this scanning protocol on two scanning positions, palm (n = 11), forearm (n = 11) and facial skin (n = 5). Based on the three scanning positions, five parameters (VAD, VSD, VDI, WTI and Young's modulus) were calculated to evaluate the biomechanical properties of the skin. Meanwhile, one facial lesion dataset was acquired to compare with healthy facial skin, which showed the differences between the lesion skin and the healthy skin. Therefore, the combination of information on structural image, elastography and angiography by employing this new scanning protocol provides potential benefits for skin disease research.

Acknowledgments. Zhengshuyi would like to thank Mr. Weiyi Jiang, Mr. Jiacheng Gu and Mr. Yu Tang for their help during data collection.

Disclosures. The authors declare no conflicts of interest.

Data availability. Data underlying the results presented in this paper are not publicly available at this time but may be obtained from the authors upon reasonable request.

References

1. PAJ Kolarsick, MA Kolarsick, and C. Goodwin, "Anatomy and Physiology of the Skin," Journal of the Dermatology Nurses' Association. **3**(4), 203–213 (2011).
2. I. Peate, "The skin: largest organ of the body," British Journal of Healthcare Assistants **15**(9), 446–451 (2021).
3. R. J. Hay, N. E. Johns, H. C. Williams, *et al.*, "The Global Burden of Skin Disease in 2010: An Analysis of the Prevalence and Impact of Skin Conditions," J. Invest. Dermatol. **134**(6), 1527–1534 (2014).
4. U. Baran, Y. Li, W. J. Choi, *et al.*, "High resolution imaging of acne lesion development and scarring in human facial skin using OCT-based microangiography," Lasers Surg. Med. **47**(3), 231–238 (2015).
5. JL Gennisson, T Baldeweck, M Tanter, *et al.*, "Assessment of elastic parameters of human skin using dynamic elastography," IEEE Trans. Ultrason., Ferroelect., Freq. Contr. **51**(8), 980–989 (2004).
6. G. Joachim and S. Acorn, "Life with a rare chronic disease: the scleroderma experience," Journal of Advanced Nursing **42**(6), 598–606 (2003).
7. A. Bono, E. Tolomio, S. Trincone, *et al.*, "Micro-melanoma detection: a clinical study on 206 consecutive cases of pigmented skin lesions with a diameter ≤ 3 mm: Micro-melanoma detection," Br. J. Dermatol. **155**(3), 570–573 (2006).
8. M. Sadeghi, T. K. Lee, D. McLean, *et al.*, "Detection and Analysis of Irregular Streaks in Dermoscopic Images of Skin Lesions," IEEE Trans. Med. Imaging **32**(5), 849–861 (2013).
9. J Dinnes, JJ Deeks, N Chuchu, *et al.*, *Dermoscopy, with and without Visual Inspection, For Diagnosing Melanoma In Adults,* Cochrane Skin Group, editor, Cochrane Database of Systematic Reviews (2018).
10. H Kittler, H Pehamberger, K Wolff, *et al.* Diagnostic accuracy of dermoscopy.
11. P. Pongkulkiat, B. Thinkhamrop, A. Mahakkanukrauh, *et al.*, "Skin model for improving the reliability of the modified Rodnan skin score for systemic sclerosis," BMC Rheumatol **6**(1), 33 (2022).
12. R. Overbury, M. A. Murtaugh, A. Fischer, *et al.*, "Primary care assessment of capillaroscopy abnormalities in patients with Raynaud's phenomenon," Clin. Rheumatol. **34**(12), 2135–2140 (2015).
13. Y. El Miedany, S. Ismail, M. Wadie, *et al.*, "Nailfold capillaroscopy: tips and challenges," Clin. Rheumatol. **41**(12), 3629–3640 (2022).
14. L. B. Dong, Y. Z. Wei, G. P. Lan, *et al.*, "High resolution imaging and quantification of the nailfold microvasculature using optical coherence tomography angiography (OCTA) and capillaroscopy: a preliminary study in healthy subjects," Quant Imaging Med Surg **12**(3), 1844–1858 (2022).
15. S. Raab, M. Klingenstein, S. Liebau, *et al.*, "A Comparative View on Human Somatic Cell Sources for iPSC Generation," Stem Cells Int. **2014**, 1–12 (2014).
16. P. Stevenson and K. Rodins, "Improving diagnostic accuracy of skin biopsies," Aust J Gen Pract **47**(4), 216–220 (2018).
17. P. C. Alguire and B. M. Mathes, "Skin biopsy techniques for the internist," J Gen Intern Med **13**(1), 46–54 (1998).
18. J. G. M. Logger, F. M. C. Vries, P. E. J. Erp, *et al.*, "Noninvasive objective skin measurement methods for rosacea assessment: a systematic review," Br. J. Dermatol. **8**, bjd.18151 (2019).
19. M. Mogensen, L. Thrane, T. M. Joergensen, *et al.*, "Optical Coherence Tomography for Imaging of Skin and Skin Diseases," Semin. Cutaneous Med. Surg. **28**(3), 196–202 (2009).
20. E. Sattler, R. Kästle, and J. Welzel, "Optical coherence tomography in dermatology," J. Biomed. Opt **18**(6), 061224 (2013).

Biomedical Optics EXPRESS

21. M. Schmid-Wendtner, T. Hinz, L. Ehler, *et al.*, "Preoperative Characterization of Basal Cell Carcinoma Comparing Tumour Thickness Measurement by Optical Coherence Tomography, 20-MHz Ultrasound and Histopathology," Acta Derm Venerol **92**(2), 132–137 (2012).
22. T. Zhang, S. Shepherd, Z. Huang, *et al.*, "Development of an intraoral handheld optical coherence tomography-based angiography probe for multi-site oral imaging," Opt. Lett. **48**(18), 4857 (2023).
23. B. Wan, C. Ganier, X. Du-Harpur, *et al.*, "Applications and future directions for optical coherence tomography in dermatology*," Br. J. Dermatol. **184**(6), 1014 (2021).
24. B. F. Kennedy, S. H. Koh, R. A. McLaughlin, *et al.*, "Strain estimation in phase-sensitive optical coherence elastography," Biomed. Opt. Express **3**(8), 1865 (2012).
25. C Li, G Guan, Y Ling, *et al.*, "Optical coherence elastography (OCE) as a method for identifying benign and malignant prostate biopsies," In: Fujimoto JG, Izatt JA, Tuchin VV, editors. San Francisco, California, United States; 2015. p. 93122S.
26. C Li, G Guan, Z Huang, *et al.*, *Full skin quantitative optical coherence elastography achieved by combining vibration and surface acoustic wave methods.* In: Tuchin VV, Larin KV, Leahy MJ, Wang RK, editors. San Francisco, California, United States; 2015. p. 93220O.
27. C. Li, G. Guan, R. Reif, *et al.*, "Determining elastic properties of skin by measuring surface waves from an impulse mechanical stimulus using phase-sensitive optical coherence tomography," J. R. Soc. Interface. **9**(70), 831–841 (2012).
28. C. Li, G. Guan, Y. Ling, *et al.*, "Detection and characterisation of biopsy tissue using quantitative optical coherence elastography (OCE) in men with suspected prostate cancer," Cancer Lett. **357**(1), 121–128 (2015).
29. T Zhang, Z Feng, Y Zhang, *et al.*, "Piezoelectrical Micro-Tapper based Three-Dimensional Optical Coherence Elastography for In Vivo Dermatology Applications," In: *2024 IEEE Ultrasonics, Ferroelectrics, and Frequency Control Joint Symposium (UFFC-JS)*. Taipei, Taiwan: IEEE; 2024. p. 1–4.
30. Z. Feng, Y. Zhang, W. Jiang, *et al.*, "Effects of Excitation Angle on Air-Puff-Stimulated Surface Acoustic Wave-Based Optical Coherence Elastography (SAW-OCE)," Photonics **11**(3), 254 (2024).
31. K Zhou, N Le, Z Huang, *et al.*, "High-intensity-focused ultrasound and phase-sensitive optical coherence tomography for high resolution surface acoustic wave elastography," J. Biophotonics. **11**(2), e201700051 (2018).
32. S. Wang, J. Li, R. K. Manapuram, *et al.*, "Noncontact measurement of elasticity for the detection of soft-tissue tumors using phase-sensitive optical coherence tomography combined with a focused air-puff system," Opt. Lett. **37**(24), 5184 (2012).
33. Y. Cheng, L. Guo, C. Pan, *et al.*, "Statistical analysis of motion contrast in optical coherence tomography angiography," J. Biomed. Opt **20**(11), 116004 (2015).
34. L. Guo, R. Shi, C. Zhang, *et al.*, "Optical coherence tomography angiography offers comprehensive evaluation of skin optical clearing *in vivo* by quantifying optical properties and blood flow imaging simultaneously," J. Biomed. Opt **21**(8), 081202 (2016).
35. A. J. Deegan, F. Talebi-Liasi, S. Song, *et al.*, "Optical coherence tomography angiography of normal skin and inflammatory dermatologic conditions," Lasers Surg. Med. **50**(3), 183–193 (2018).
36. A. J. Deegan, W. Wang, S. Men, *et al.*, "Optical coherence tomography angiography monitors human cutaneous wound healing over time," Quant. Imaging Med. Surg. **8**(2), 135–150 (2018).
37. J. Lu, A. J. Deegan, Y. Cheng, *et al.*, "OCT-Based Angiography and Surface Topography in Burn-Damaged Skin," Lasers Surg. Med. **53**(6), 849–860 (2021).
38. T. Zhang, Y. Zhang, J. Liao, *et al.*, "Quantitative assessment of the oral microvasculature using optical coherence tomography angiography," Front. Bioeng. Biotechnol. **12**, 1464562 (2024).
39. R. Reif, J. Qin, L. An, *et al.*, "Quantifying Optical Microangiography Images Obtained from a Spectral Domain Optical Coherence Tomography System," Int. J. Biomed. Imaging **2012**, 1–11 (2012).
40. Z. Chu, J. Lin, C. Gao, *et al.*, "Quantitative assessment of the retinal microvasculature using optical coherence tomography angiography," J. Biomed. Opt **21**(6), 066008 (2016).
41. F. Martelli and C. Giacomozzi, "Tortuosity Index Calculations in Retinal Images: Some Criticalities Arising from Commonly Used Approaches," Information **12**(11), 466 (2021).
42. T. T. Hormel, J. Wang, S. T. Bailey, *et al.*, "Maximum value projection produces better en face OCT angiograms than mean value projection," Biomed. Opt. Express **9**(12), 6412 (2018).
43. AF Frangi, WJ Niessen, KL Vincken, *et al.*, "Multiscale vessel enhancement filtering," In: Wells WM, Colchester A, Delp S, editors. *Medical Image Computing and Computer-Assisted Intervention — MICCAI'98* (Springer Berlin Heidelberg, 1998), p. 130–7. (Lecture Notes in Computer Science; vol. 1496).
44. D. Bradley and G. Roth, "Adaptive Thresholding using the Integral Image," Journal of Graphics Tools **12**(2), 13–21 (2007).
45. N. Otsu, "A Threshold Selection Method from Gray-Level Histograms," IEEE Trans. Syst., Man, Cybern. **9**(1), 62–66 (1979).
46. S Song, Z Huang, TM Nguyen, *et al.*, "Shear modulus imaging by direct visualization of propagating shear waves with phase-sensitive optical coherence tomography," J. Biomed. Opt. **18**(12), 1 (2013).
47. M. A. Kirby, P. Tang, H. C. Liou, *et al.*, "Probing elastic anisotropy of human skin in vivo with light using non-contact acoustic micro-tapping OCE and polarization sensitive OCT," Sci. Rep. **12**(1), 3963 (2022).
48. C. Li, G. Guan, X. Cheng, *et al.*, "Quantitative elastography provided by surface acoustic waves measured by phase-sensitive optical coherence tomography," Opt. Lett. **37**(4), 722 (2012).

Biomedical Optics EXPRESS

49. S. J. Men, C. Chen, W. Wei, *et al.*, "Repeatability of vessel density measurement in human skin by OCT -based microangiography," Skin Research and Technology **23**(4), 607–612 (2017).
50. S. Es'haghian, K. M. Kennedy, P. Gong, *et al.*, "In vivo volumetric quantitative micro-elastography of human skin," Biomed. Opt. Express **8**(5), 2458 (2017).
51. K. Zhou, K. Feng, C. Li, *et al.*, "A Weighted Average Phase Velocity Inversion Model for Depth-Resolved Elasticity Evaluation in Human Skin In-Vivo," IEEE Trans. Biomed. Eng. **68**(6), 1969–1977 (2021).
52. X. Zhang, T. G. Osborn, M. R. Pittelkow, *et al.*, "Quantitative assessment of scleroderma by surface wave technique," Medical Engineering & Physics **33**(1), 31–37 (2011).
53. A. Wakhlu, A. Chowdhury, N. Mohindra, *et al.*, "Assessment of extent of skin involvement in scleroderma using shear wave elastography," Indian J Rheumatol **12**(4), 194–198 (2017).
54. G Boyer, H Zahouani, Le Bot, *et al.*, "In vivo characterization of viscoelastic properties of human skin using dynamic micro-indentation," In: *2007 29th Annual International Conference of the IEEE Engineering in Medicine and Biology Society*. IEEE:Lyon, France 2007, p. 4584.
55. S. I. Yum and J. Roe, "Capillary Blood Sampling for Self-Monitoring of Blood Glucose," Diabetes Technol. Ther. **1**(1), 29–37 (1999).
56. Z. Xie, N. Zeinstra, M. A. Kirby, *et al.*, "Quantifying Microvascular Structure in Healthy and Infarcted Rat Hearts Using Optical Coherence Tomography Angiography," IEEE Trans. Med. Imaging **43**(8), 2878–2887 (2024).
57. D. C. Chong, Z. Yu, H. E. Brighton, *et al.*, "Tortuous Microvessels Contribute to Wound Healing via Sprouting Angiogenesis," Arterioscler., Thromb., Vasc. Biol. **37**(10), 1903–1912 (2017).